

A Model of Laser-Powder Interaction in Direct Selective Laser Sintering of Metals

Suman Das and Haseung Chung
Department of Mechanical Engineering
University of Michigan
Ann Arbor, MI 48109-2125

Abstract

We present a simple one-dimensional model that describes the physical mechanisms of heat transfer, melting and resolidification taking place during and after the interaction of a laser beam with a bed of pure metal powder. The physical model describing this situation is based on the classical Stefan problem with appropriately chosen boundary conditions to reflect direct selective laser sintering of metals. A numerical model based on the finite volume method is developed to perform computations for two beam diameters, three beam speeds and for constant, step and ramp laser power input profiles. The results of these computations show the influence of laser beam diameter, laser power input rate and input duration on the melt interface velocity and location, and temperature. Scaling laws for time to reach maximum melt depth and total melt-resolidification time are derived. Comparisons of the temperature histories for the three power input profiles are described.

INTRODUCTION

Selective laser sintering (SLS) is a solid freeform fabrication [1] technique that creates three-dimensional freeform objects directly from their CAD models. An object is created by selectively fusing thin layers of a powder using a computer-controlled scanning laser beam that scans patterns corresponding to slices of the CAD model. Direct selective laser sintering of metals [2] is a process in which a high-energy laser beam directly consolidates a metal powder or powder mixture to full density. Direct selective laser sintering of metals is a complex process exhibiting multiple modes of heat, mass and momentum transfer, and chemical reaction mechanisms. The strong interplay between these mechanisms directly impacts the SLS process, determining whether a given material can be processed and if so, how the microstructure and properties of the material are impacted. The inherent complexity of this process imposes serious constraints on the complexity of the models that can be constructed to enable a fundamental understanding of the important physical mechanisms in SLS. This understanding is essential to implement effective process control.

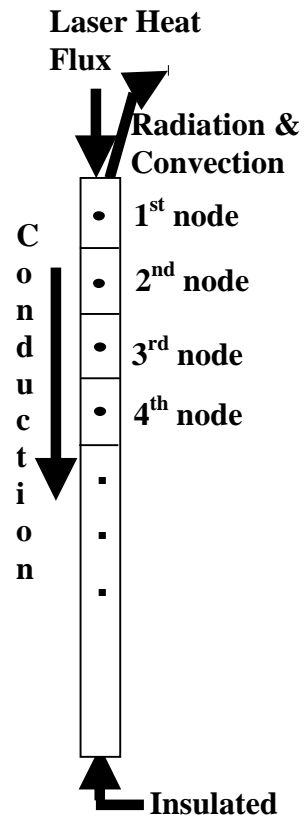
Previous work on modeling SLS of metals includes finite element modeling for metal powder densification [3] and three dimensional models for two-component metal mixtures [4]. With the goal of developing process understanding for control purposes, we present a simple one-dimensional model that describes the physical mechanisms of heat transfer, melting and resolidification taking place during and after the interaction of a laser beam with a bed of pure metal powder. The physical model describing this situation is based on the classical Stefan problem with appropriately chosen boundary conditions to reflect direct selective laser sintering of metals. A numerical model based on the finite volume method was developed to perform computations for two beam diameters, three beam speeds and for constant, step and ramp laser power input profiles. Properties of nickel were used for the numerical computations. The results of these computations show the influence of laser beam diameter, laser power input rate and input duration on the melt interface velocity and location, and temperature. Scaling laws for time

to reach maximum melt depth and total melt-resolidification time are derived. Comparisons of the temperature histories for the three power input profiles are described.

PHYSICAL MODEL

We consider one-dimensional heat conduction in a solid of length L . Heat flux from the laser flows in through the surface at $x=0$ at a rate q'' per unit area during heat up while the surface at $x = L$ is assumed insulated. If heating continues long enough, the surface at $x = 0$ reaches the melting temperature T_m , melting commences and the melt interface moves inward. This is the well documented Stefan problem [5,6]. During cool down, heat is lost from the surface at $x=0$ by convection and radiation. We aim to determine the temperature distribution, the velocity and the location of the melting interface within the domain of interest. The following assumptions are made for developing the model:

1. Powder is treated as a solid, no densification occurs during the process.
2. Laser beam intensity distribution is uniform across the beam diameter.
3. Constant material properties.
4. No convective heat transfer at top surface (process occurs in a vacuum).
5. No melt pool convection, no convective heat transfer at melt interface.
6. Planar propagation of melt interface.
7. No evaporative heat loss and no evaporative mass transfer at top surface.
8. Top surface is diffuse gray, top surface cools by radiative cooling.



The governing heat equation describing the process is as follows:

$$\frac{\partial}{\partial x} \left(k \frac{\partial T}{\partial x} \right) + \frac{\partial}{\partial y} \left(k \frac{\partial T}{\partial y} \right) + \frac{\partial}{\partial z} \left(k \frac{\partial T}{\partial z} \right) + \dot{q} = \rho c_p \frac{\partial T}{\partial t}$$

The one-dimensional form of this equation with constant properties is

$$k \frac{\partial^2 T}{\partial x^2} = \rho c_p \frac{\partial T}{\partial t} \quad (1)$$

During heat up and melting, the heat flux boundary condition at the top surface is

$$-k \frac{\partial T}{\partial x} = \alpha_a q'', x = 0 \quad (2)$$

During cool down, the general convection and radiation boundary condition at the top surface is

$$-k \frac{\partial T}{\partial x} = h(T_\infty - T) + \epsilon \sigma (T_\infty^4 - T^4), x = 0 \quad (3)$$

The bottom surface is assumed insulated, therefore the boundary condition there is

$$-k \frac{\partial T}{\partial x} = 0, x = L \quad (4)$$

The Stefan condition describing the heat flux balance at the planar melt interface is

$$k \frac{\partial T}{\partial x} \Big|_s - k \frac{\partial T}{\partial x} \Big|_l = \rho V \lambda, x = x_f \quad (5)$$

NUMERICAL MODEL

The finite volume method [7] is employed to develop the numerical model. The computational domain is divided into $2N$ cells and a node is placed at the center of each cell. Symmetry is used to accommodate the insulation boundary condition. Using symmetry, computation is done only for the first $N+1$ nodes. The 1st node and $(N+1)$ th node are used to satisfy the boundary conditions. The temperatures computed at each node represent average temperatures for the cell (finite volume element) corresponding that node.

Temperature computation at an interior node not adjacent to the melt interface is given by

$$\rho c \delta x \frac{dT_i}{dt} = \frac{k}{\delta x} (T_{i-1} - T_i) + \frac{k}{\delta x} (T_{i+1} - T_i) \quad (6)$$

which can be rewritten as

$$\frac{\delta x^2}{\alpha} \frac{dT_i}{dt} = (T_{i-1} - T_i) + (T_{i+1} - T_i) \quad (7)$$

The time derivative of temperature can be approximated as $(T_i^{new} - T_i) / \delta t$. Substituting this into (7) and re-arranging leads to an algorithm for computing the new temperature at each node by

$$T_i^{new} = T_i + \frac{\alpha \delta t}{\delta x^2} (T_{i-1} - T_i) + \frac{\alpha \delta t}{\delta x^2} (T_{i+1} - T_i) \quad (8)$$

Temperature computation at the surface node during heat up is given by

$$\rho c \delta x \frac{dT_i}{dt} = \alpha_a q'' + \frac{2k}{\delta x} (T_{i-1} - T_i) + \frac{k}{\delta x} (T_{i+1} - T_i) \quad (9)$$

Using the time derivative of temperature approximation, (9) can be rewritten as

$$T_i^{new} = T_i + \frac{\delta t}{\rho c \delta x} \alpha_a q'' + \frac{2\alpha \delta t}{\delta x^2} (T_{i-1} - T_i) + \frac{\alpha \delta t}{\delta x^2} (T_{i+1} - T_i) \quad (10)$$

By combining the heat transfer resistances for convection, radiation, and conduction for half of δx , the temperature computation at the surface node during cool down is given by

$$\rho c \delta x \frac{dT_i}{dt} = \frac{T_{i-1} - T_i}{\frac{1}{h + \varepsilon \sigma (T_{i-1}^2 + T_i^2)(T_{i-1} + T_i)} + \frac{\delta x}{2k}} + \frac{k}{\delta x} (T_{i+1} - T_i) \quad (11)$$

which again using the time derivative of temperature approximation can be rewritten as

$$T_i^{new} = T_i + \frac{T_{i-1} - T_i}{\frac{1}{h + \varepsilon \sigma (T_{i-1}^2 + T_i^2)(T_{i-1} + T_i)} + \frac{\delta x}{2k}} \frac{\delta t}{\rho c \delta x} + \frac{\alpha \delta t}{\delta x^2} (T_{i+1} - T_i) \quad (12)$$

By symmetry, temperature computation at the end node is given by $T(N+1)=T(N)$. Hence, after $T(N)$ has been computed, we simply set $T(N+1)=T(N)$. To satisfy the Stefan condition, heat fluxes due to conduction in the solid and liquid at the previous time step are approximated by

$$k \left. \frac{\partial T}{\partial x} \right|_s = k \frac{T_{i+1} - T_m}{x_{i+1} - x_f} \quad \text{and} \quad k \left. \frac{\partial T}{\partial x} \right|_f = k \frac{T_m - T_{i-1}}{x_f - x_{i-1}} \quad \text{respectively} \quad (13)$$

while the melt front velocity is approximated by

$$V = \frac{x_f^{new} - x_f}{\delta t} \quad (14)$$

These approximations lead to an algebraic version of the Stefan condition given by

$$k \frac{T_{i+1} - T_m}{x_{i+1} - x_f} - k \frac{T_m - T_{i-1}}{x_f - x_{i-1}} = \rho \lambda \frac{x_f^{new} - x_f}{\delta t} \quad (15)$$

that can be rewritten to yield the new location of the melt interface via

$$x_f^{new} = x_f + \frac{\delta t}{\rho \lambda} \left(k \frac{T_{i+1} - T_m}{x_{i+1} - x_f} - k \frac{T_m - T_{i-1}}{x_f - x_{i-1}} \right) \quad (16)$$

A different set of equations is employed for computation in nodes adjacent to cells containing the melt interface. The discretized heat flux balance for such nodes is given by

$$\rho c \delta x \frac{dT_i}{dt} = \frac{k}{\delta x} (T_{i-1} - T_i) + \frac{k}{x_f - x_i} (T_m - T_i) \quad (17)$$

The corresponding temperature computation is given by

$$T_i^{new} = T_i + \frac{\alpha \delta t}{\delta x^2} (T_{i-1} - T_i) + \frac{\alpha \delta t}{\delta x} \frac{1}{x_f - x_i} (T_m - T_i) \quad (18)$$

When the melt interface is in the second cell, a special case arises for the first node. The temperature computation for the first node during heat up and melting is given by

$$T_i^{new} = T_i + \frac{\delta t}{\rho c \delta x} \alpha_a q'' + 2 \frac{\alpha \delta t}{\delta x^2} (T_{i-1} - T_i) + \frac{\alpha \delta t}{\delta x^2} \frac{\delta x}{x_f - x_i} (T_m - T_i) \quad (19)$$

while its temperature during cool down and re-solidification is given by

$$T_i^{new} = T_i + \frac{T_{i-1} - T_i}{\frac{1}{h + \varepsilon \sigma (T_{i-1}^2 + T_i^2) (T_{i-1} + T_i)} + \frac{\delta x}{2k}} \frac{\delta t}{\rho c \delta x} + \frac{\alpha \delta t}{\delta x^2} \frac{\delta x}{x_f - x_i} (T_m - T_i) \quad (20)$$

The discretized heat flux balance at an interior node adjacent and to the right of the melt interface is given by

$$\rho c \delta x \frac{dT_i}{dt} = \frac{k}{x_i - x_f} (T_m - T_i) + \frac{k}{\delta x} (T_{i+1} - T_i) \quad (21)$$

The corresponding temperature computation is given by

$$T_i^{new} = T_i + \frac{\alpha \delta t}{\delta x} \frac{1}{x_i - x_f} (T_m - T_i) + \frac{\alpha \delta t}{\delta x^2} (T_{i+1} - T_i) \quad (22)$$

Finally, temperature interpolation at a node after the melt interface has passed by it is given by

$$T_i = T_{i-1} + (x_i - x_{i-1}) \frac{T_m - T_{i-1}}{x_m - x_{i-1}} \quad (23)$$

The parameter values used for the computations are shown in table 1.

| Domain size | Number of nodes | Time step | Laser beam power | Beam diameter |
|-------------|-----------------|------------------------|------------------|----------------|
| 2 mm | 100 | 4 x 10 ⁻⁶ s | 500 W | 100 μm, 250 μm |

Table 1. Parameters used for numerical computations.

The concept of beam-material interaction time is used to simulate the temporal action of a moving laser beam over a surface area corresponding to one beam diameter. The beam-material interaction time is defined as the time taken by the beam to traverse one beam diameter, and can be used to set the duration for step power input and ramp power input experienced by an area of the surface corresponding to one beam diameter. Three typical beam speeds in SLS processing of

metals [6] were chosen to determine beam-material interaction times for each of the 100 μm and 250 μm beam diameters used in the computations, as shown in table 2.

| Beam speed (in/s) | $t_f=d/v$ (100 μm beam) | $t_f=d/v$ (250 μm beam) |
|-------------------|---------------------------------------|---------------------------------------|
| 5 (12.7 cm/s) | 7.87×10^{-4} sec | 1.97×10^{-3} sec |
| 10 (25.4 cm/s) | 3.94×10^{-4} sec | 9.84×10^{-4} sec |
| 50 (127 cm/s) | 7.87×10^{-5} sec | 1.97×10^{-4} sec |

Table 2. Beam-material interaction times for step power input and ramp power input

RESULTS AND DISCUSSION

Numerical computations were conducted for three types of laser power input; constant power input (laser beam always on), step power input (constant laser power for the duration of beam-material interaction time followed by a drop to zero power) and ramp power input (laser power linearly ramps from zero to full power during beam-material interaction time, followed by a drop to zero power), for two beam diameters (100 μm and 250 μm). For the step and ramp power inputs, computations were carried out for three beam-material interaction times with durations equal to five times beam-material interaction time. Plots of interface velocity, interface location, surface temperature and center node temperature were obtained. The results for each case are described in the following sections.

Case I: Constant Power Input

Figure 1 shows the interface velocity and location as a function of time for constant power input with a 100 μm beam. The interface velocity initially peaks to nearly 4 m/s but then drops sharply to nearly zero in 5×10^{-3} s. The interface location continues to penetrate deeper into the solid during this time as is expect for constant heat flux input, reaching a final value of 460 μm .

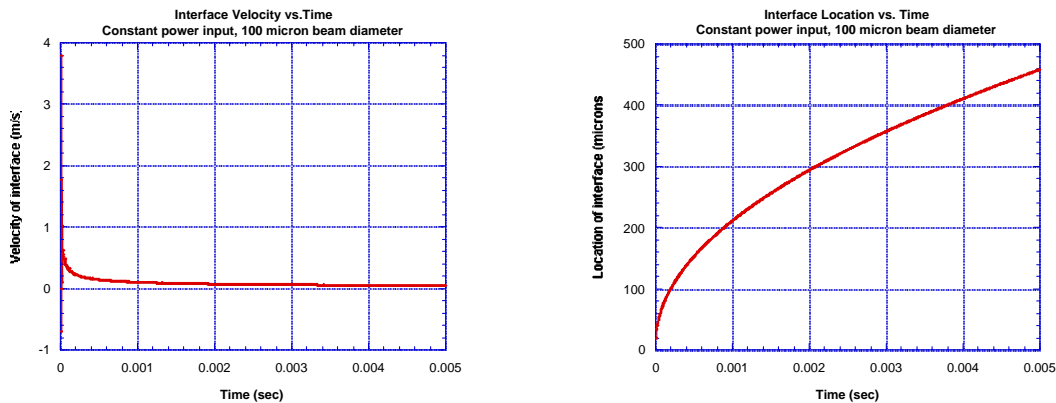


Fig.1. Interface velocity and location for 100 μm beam and constant power input.

Figure 2 shows surface and center node temperatures for constant power input. The computed peak surface temperatures for 100 μm are very high (much higher than the melting point of nickel), which are attributed to unmodeled effects (e.g. evaporation and melt pool convection). At 5 ms, the temperature half-way (1 mm) into the computational domain is lower than the surface temperature by a factor of about 3, yielding a temperature gradient of about 4000 K/mm.

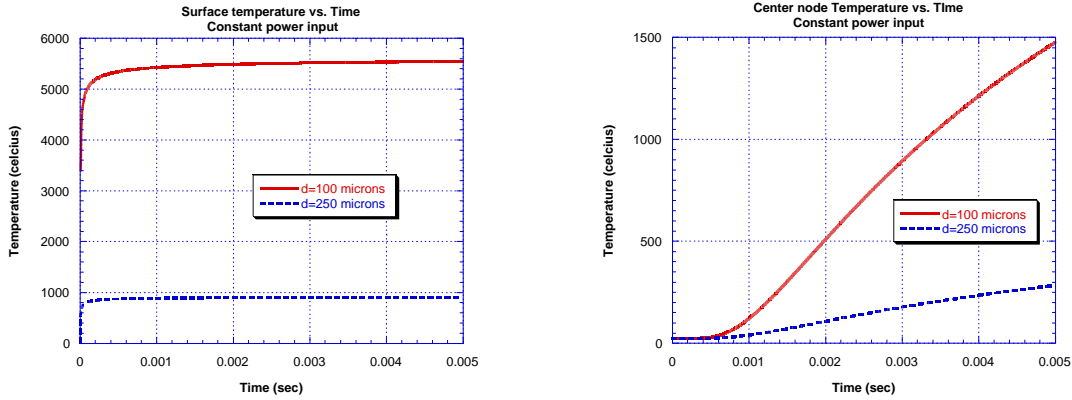


Fig. 2. Surface and center node temperatures for 100 μm beam and constant power input.

Case II: Step Power Input

Figure 3 shows interface velocity and location for 100 μm beam for the three beam-material interaction times and step power input. The variation of interface velocity with time is not significantly different for the three cases. However, the maximum melt penetration depth and time at which the interface velocity changes sign are proportional to beam-material interaction time. The time to reach maximum melt depth scales with the beam-material interaction time by a constant factor of about 2. Estimates for the total melt-resolidification times can be obtained by linearly extrapolating the downward (resolidification) portions of the interface location curves to intersect the X-axis. By these estimates, the total melt-resolidification time scales with the corresponding beam-material interaction time by a constant factor of about 10, i.e. about one order of magnitude.

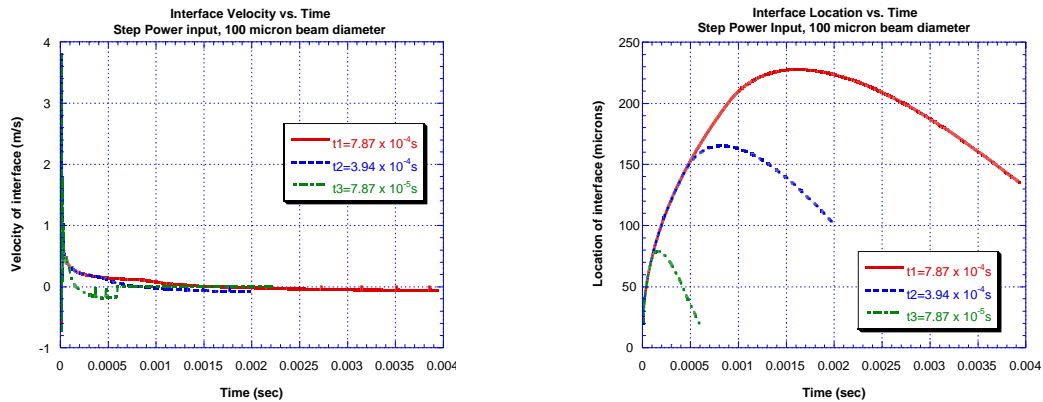


Fig. 3. Interface velocity and location for 100 μm beam and step power input.

Figure 4 shows the surface and center node temperatures for 100 μm beam diameter for the three beam-material interaction times and step power input. As in the case of constant power input, the computed peak surface temperatures are very high, reflecting unmodeled effects. The peak temperature is proportional to the beam-material interaction time. Surface cooling begins almost instantaneously as the power is turned off, and the associated cooling rate is inversely proportional to beam-material interaction time. At the end of beam-material interaction, the temperature half-way (1 mm) into the computational domain has barely risen from ambient and the temperature gradient relative to the surface is about 5000 K/mm for all three instances of beam-material interaction time.

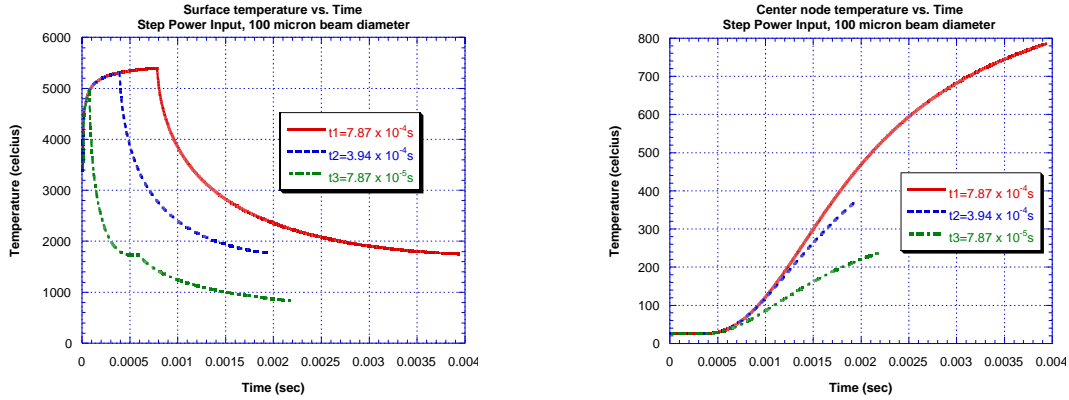


Fig. 4. Surface and center node temperatures for 100 μm and step power input.

Case III: Ramp Power Input

Figure 5 shows interface velocity and location for 100 μm beam for the three beam-material interaction times and ramp power input. The peak interface velocity is inversely proportional while the time to reach the peak velocity is directly proportional to beam-material interaction time respectively. The maximum melt penetration depth and time at which the interface velocity changes sign are proportional to beam-material interaction time. The time to reach maximum melt depth scales with the beam-material interaction time by a constant factor of about 1.4. Estimates for the total melt-resolidification times can be obtained by linearly extrapolating the downward (resolidification) portions of the interface location curves to intersect the X-axis. By these estimates, the total melt-resolidification time scales with the corresponding beam-material interaction time by a constant factor of about 4.

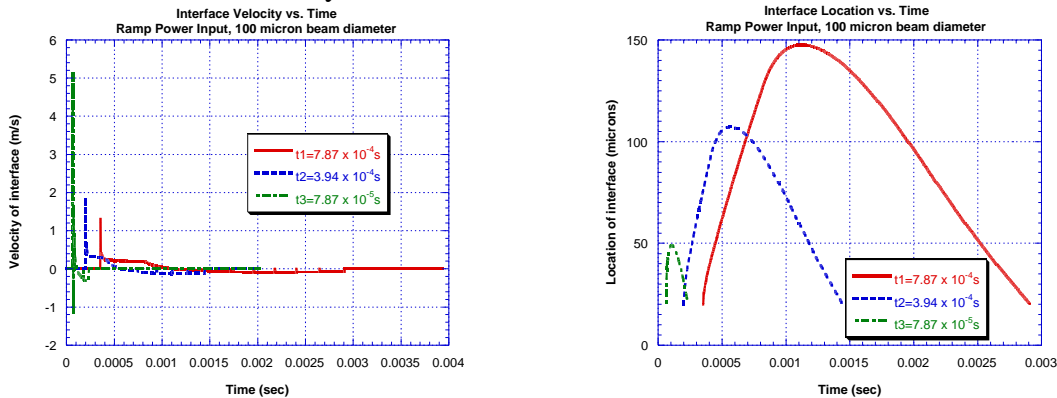


Fig. 5. Interface velocity and location for 100 μm and ramp power input.

Figure 6 shows the surface and center node temperatures for 100 μm beam diameter for the three beam-material interaction times and ramp power input. The peak temperature is proportional to the beam-material interaction time while the rate of surface temperature rise is inversely proportional to beam-material interaction time. Surface cooling begins almost instantaneously as the power is turned off, and the associated cooling rate is inversely proportional to beam-material interaction time. The predicted peak temperatures are comparable to those predicted for constant power and step input power, but are again high, reflecting unmodeled effects. At the end of beam-material interaction, the temperature half-way (1 mm) into the computational domain has barely risen from ambient and the temperature gradient

relative to the surface is between 4000 K/mm and 5000 K/mm for all three instances of beam-material interaction time.

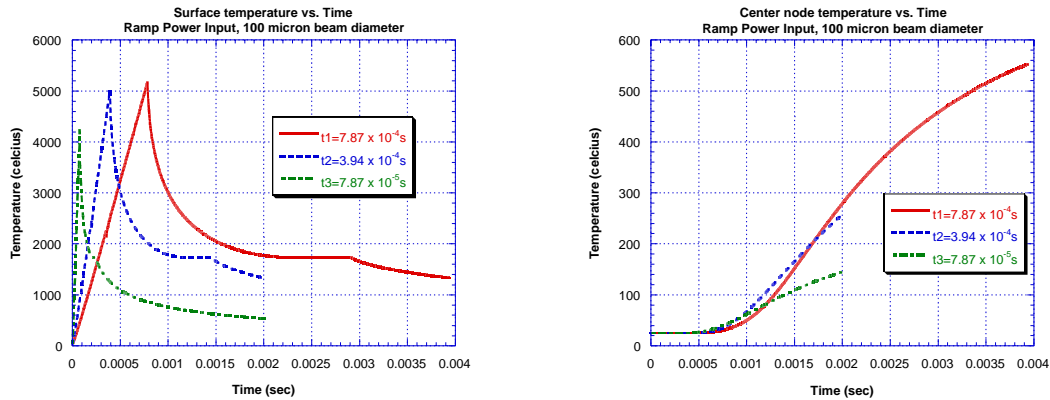


Fig. 6 Surface and center node temperatures for 100 μm and ramp power input.

Figure 7 shows comparisons of surface temperature for constant, step and ramp power inputs with respect to beam diameter for a beam-material interaction time corresponding to 12.7 cm/s (5 in/s) beam speed. No melting is predicted for a 250 μm beam in all cases. The predicted peak temperatures for all three types of power input are nearly the same with constant power input providing the highest temperature as expected, followed by step power input and ramp power input. The rate of temperature rise for ramp power input is more gradual versus step power input as expected. However, the cooling curves are nearly identical for both step and ramp power input.

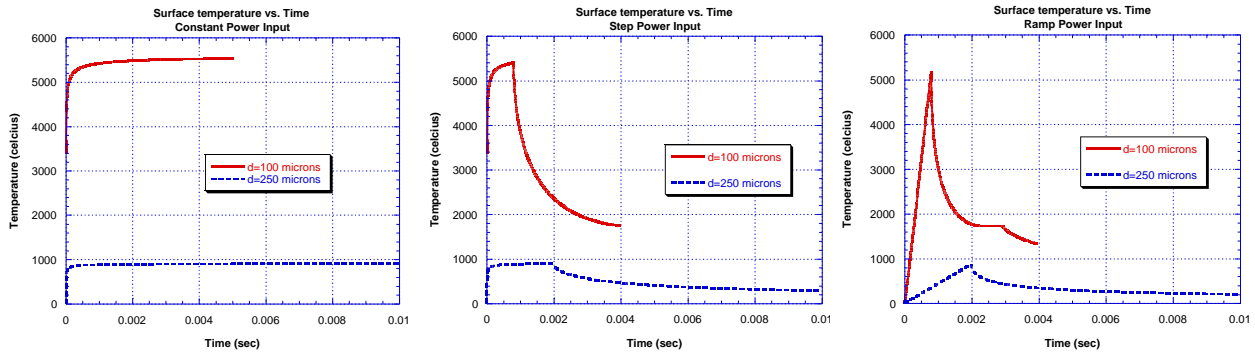


Fig. 7. Surface temperature comparisons for constant power, step power and ramp power at 5 in/s.

SUMMARY AND CONCLUSIONS

The results from this preliminary model can be summarized as follows:

1. No melting is predicted for the 250 μm beam for all cases. The predicted surface temperatures, especially for 100 μm beam are very high, reflecting unmodeled effects (e.g. evaporative heat loss, melt pool convection, temperature dependent properties).
2. For the same beam-material interaction time (same beam speed), peak temperatures for both step and ramp power inputs are inversely proportional to beam diameter.
3. For both step and ramp power input, the peak interface velocity and surface cooling rate after terminating laser power input are inversely proportional to beam-material interaction time while the time to reach peak interface velocity is directly proportional to beam-material interaction time.

4. Peak temperatures for both step and ramp power inputs are attained at the end of beam-material interaction time.
5. For step and ramp power inputs, the maximum melt penetration depth and time at which the interface velocity changes sign (start of resolidification) are proportional to beam-material interaction time.
6. For the same beam-material interaction time, beam diameter and laser power, the maximum melt depth for step power input is higher than that for ramp power input.
7. For step power input, the time to reach maximum melt depth scales with the beam-material interaction time by a factor of about 2 while the total melt-resolidification time scales with the corresponding beam-material interaction time by a factor of about 10.
8. For ramp power input, the time to reach maximum melt depth scales with the beam-material interaction time by a factor of about 1.4 while the total melt-resolidification time scales with the corresponding beam-material interaction time by a factor of about 4.

REFERENCES

1. Beaman, J. J., Barlow, J. W., Bourell, D. L., Crawford, R. H., Marcus H. L., and McAlea, K. P., *Solid Freeform Fabrication: A New Direction in Manufacturing*, Kluwer Academic Publishers, 1997.
2. Suman Das, *Direct Selective Laser Sintering of High Performance Metals-Machine Design, Process Development and Process Control*, Ph.D. dissertation, The University of Texas at Austin, 1998.
3. Shiomi, M., Yoshidome, A., Abe, F., and Osakada, K., "Finite element analysis of melting and solidifying processes in laser rapid prototyping of metallic powders", *International Journal of Machine Tools & Manufacture*, Vol. 39, 1999, pp. 237-252.
4. Zhang, Y., Faghri, A., Buckley, C. W., and Bergman, T. L., "Three-Dimensional Sintering of Two-Component Metal Powders With Stationary and Moving Laser Beams", *ASME J. Heat Transfer*, Vol. 122, 2000, pp. 150-158.
5. Cohen, M. I., 1967, "Melting of a Half-Space Subjected to a Constant Heat Input", *Journal of The Franklin Institute*, Vol. 283, 1967, pp. 271-285.
6. Landau, H. G., "Heat Conduction In a Melting Solid", *Quarterly of Applied Mathematics*, Vol. 8, 1950, pp. 81-94.
7. Patankar, S. V., *Numerical Heat Transfer and Fluid Flow*, 1980, Taylor & Francis.

NOMENCLATURE

Symbols

c_p = specific heat (J/kgK)
 d = beam diameter (m)
 h = convective heat transfer coefficient (W/m²K)
 k = thermal conductivity (W/mK)
 \dot{q} = internal heat generation (W/m³)
 q'' = heat flux (W/m²)
 T_m = melting temperature (K)
 T_{oo} = ambient temperature (K)
 T_i = temperature at node (K)
 x_i = location of node (m)
 x_f = location of interface (m)
 v = beam speed (m/s)
 V = melt front velocity (m/s)

Greek Letters

α_a = absorptivity of surface
 (assumed 0.8 for nickel)
 α = thermal diffusivity (m²/s)
 δt = interval time (s)
 δx = distance between nodes (m)
 ϵ = emissivity of surface
 (assumed 0.8 for nickel)
 λ = latent heat of fusion (kJ/kg)
 ρ = density (kg/m³)
 σ = Stefan-Boltzmann constant